

# High-Performance Si Photocathode Enabled by Spatial Decoupling Multifunctional Layers for Water Splitting

Zongwei Mei, Yongji Chen, Shengfu Tong, Yang Li, Jian Liu, Lizhi Sun, Wu Zhong, Xinyan Dong, Yuchen Ji, Yuan Lin, Haibiao Chen, and Feng Pan\*

Spatial decoupling of light absorption and catalytic reaction is a promising approach to improve the efficiency and stability of Si photoelectrodes. Herein, patterned Ag dots (PADs) are fabricated as the front electrode on a glass layer on commercial SiN<sub>y</sub>-coated monocrystalline p-n<sup>+</sup> Si by an industrial manufacture strategy. It is found that the electron tunneling glass layer offers excellent protection to Si photocathode in an acidic electrolyte (0.5 M H<sub>2</sub>SO<sub>4</sub>). The SiN<sub>x</sub> layer for antireflection and surface passivation also resists the corrosive electrolyte. Under 1 sun (AM 1.5G) illumination, PADs-decorated photocathode with a 0.75 mm dot-spacing exhibits a saturation photocurrent of 36.1 mA cm<sup>-2</sup> and a photovoltage of 0.61 V when Pt is electrodeposited as the hydrogen evolution catalyst on PADs. The applied bias photo-to-current conversion efficiency (ABPE) reaches 9.7%. This performance is enabled by the simultaneous optimization of light absorption and collection of photoexcited electrons. The photocurrent can remain stable for about 100 h at 0 V versus the reversible hydrogen electrode (RHE). This study identifies a new combination of multifunctional spatial-decoupling layers that is efficient in both light absorption, transfer of photoexcited electrons, and stable in an acidic electrolyte.

Z. Mei, Y. Chen, Y. Li, J. Liu, L. Sun, W. Zhong, X. Dong, Y. Ji, F. Pan School of Advanced Materials Peking University Shenzhen Graduate School, Shenzhen 518055, China E-mail: panfeng@pkusz.edu.cn

7 Mei

Yangtze Delta Region Institute (Huzhou) & School of Physics University of Electronic Science and Technology of China Huzhou 313001, China

S. Tong Jinhua Advanced Research Institute Jinhua 321013, China

Y. Lin Institute of Chemistry Chinese Academy of Sciences Beijing 100190, China

H. Chen Institute of Marine Biomedicine Shenzhen Polytechnic Shenzhen 518055, China

F. Pan
Chemistry and Chemical Engineering Guangdong Laboratory
Shantou 515031, China

The ORCID identification number(s) for the author(s) of this article can be found under https://doi.org/10.1002/adfm.202107164.

DOI: 10.1002/adfm.202107164

#### 1. Introduction

Photoelectrochemical (PEC) water splitting by solar irradiation is a promising approach to transfer intermittent solar energy into green, renewable, and storable H<sub>2</sub> fuel.<sup>[1]</sup> The research goals for a practical photoelectrode include high efficiency, long-term stability, and low cost.[2,3] Over the past decades, many semiconductorbased photoanodes have been developed, and the underlying materials include WO<sub>3</sub>,<sup>[4]</sup> Fe<sub>2</sub>O<sub>3</sub>,<sup>[5]</sup> BiVO<sub>4</sub>,<sup>[6]</sup> (oxy)nitrides,<sup>[7]</sup> metal sulfides,<sup>[8]</sup> and other ternary metal oxides.<sup>[9]</sup> Tremendous efforts have also been dedicated to study p-type metal oxides or metal chalcogenides as photocathodes.[10] However, most photoelectrodes mentioned above still suffer from poor performance due to limited light absorption and/or quick recombination of photoexcited carriers.[6,7,9,10] Additionally, plenty of organic or hybrid organic-

inorganic photoelectrodes have also been applied to water splitting.<sup>[11–21]</sup> Great improvement of efficiency and stability is the key issue for these organic-based photoelectrodes at the present stage. Semiconductor Si with a narrow band gap (1.12 eV) can efficiently absorb the solar light and the photoconversion efficiency has reached over 26% in photovoltaic solar cell.<sup>[3,22]</sup> Intense research has also been focused on Si photoelectrodes for PEC water splitting because it is possible to maintain a low fabrication cost with the existing Si solar cell industry. The key to successful Si photoelectrodes is to improve efficiency and stability.<sup>[1–3,23–29]</sup>

To protect the Si photoelectrode from the corrosion by the electrolyte, a pinhole-free surface layer which is highly transparent and also allows tunneling or conduction of electrons is vital. Protection layers of metal (Pt, Co, or Ni),  $^{[1,25,30]}$  SrTiO<sub>3</sub>,  $^{[3]}$  NiO<sub>x</sub>,  $^{[31]}$  Co<sub>3</sub>O<sub>4</sub>,  $^{[23]}$  and TiO<sub>2</sub>  $^{[2,27-29]}$  have been proved to be successful for enabling efficient and comparatively stable Si photoelectrodes in corrosive electrolytes. However, usually, the layer has to be thick enough to provide satisfactory protection, while a thick layer is detrimental to charge migration and light transmission, resulting in a low photovoltage and a low photocurrent density.  $^{[32]}$  A viable solution to this dilemma is to spatially separate the part for light absorption and the part for catalytic reactions.  $^{[3,26,33]}$  The light absorption part needs a more stable protection layer with high light transmission like

www.afm-iournal.de

16163028, 2022. 2, Downloaded from https://advanced.onlinelibrary.wiley.com/doi/10.1002/adfm.202107164 by University Town Of Shenzhen, Wiley Online Library on [23/11/2025]. See the Terms and Conditions (https://onlinelibrary.wiley.com/doi/10.1002/adfm.202107164 by University Town Of Shenzhen, Wiley Online Library on [23/11/2025]. See the Terms and Conditions (https://onlinelibrary.wiley.com/doi/10.1002/adfm.202107164 by University Town Of Shenzhen, Wiley Online Library on [23/11/2025]. See the Terms and Conditions (https://onlinelibrary.wiley.com/doi/10.1002/adfm.202107164 by University Town Of Shenzhen, Wiley Online Library on [23/11/2025]. See the Terms and Conditions (https://onlinelibrary.wiley.com/doi/10.1002/adfm.202107164 by University Town Of Shenzhen, Wiley Online Library on [23/11/2025]. See the Terms and Conditions (https://onlinelibrary.wiley.com/doi/10.1002/adfm.202107164 by University Town Of Shenzhen, Wiley Online Library on [23/11/2025].

on Wiley Online Library for rules of use; OA articles are governed by the applicable Creative Commons

 $\mathrm{SiN}_{x}$ . [34–36] Simultaneously, the protection layer in the reaction part should facilitate efficient charge transfer. Till now, the fabrication of such layers usually needs complex procedures and few researches have adopted a scalable manufacturing route for the Si photoelectrode. [1–3,23,25,27–29]

In this work, we fabricated patterned Ag dots (PADs) with different dot-spacings on commercial monocrystalline p-n<sup>+</sup> Si wafer with a  $\mathrm{SiN}_x$  coating (**Figure 1A**) using a scalable manufacturing strategy on an Applied Baccini Soft Line (see Supporting Information). This equipment is widely used in the Si solar cell wafer fabrication industry. After screen printing and heat treatment, the  $\mathrm{SiN}_x$  layer was etched by the silver paste and a glass layer was produced between the n-type Si and the printed Ag (Figure 1B). The commercial silver paste used in this work contains glass frits made of PbO,  $\mathrm{Bi}_2\mathrm{O}_3$ ,  $\mathrm{TeO}_2$ ,  $\mathrm{B}_2\mathrm{O}_3$ , and  $\mathrm{SiO}_2$  et al. Previous in situ X-ray diffraction (XRD) during firing revealed that the PbO in the glass frits etched the  $\mathrm{SiN}_x$  antireflective coating between 500 and 650 °C as described by: $^{[37]}$ 

$$2PbO + SiN_x \rightarrow 2Pb + SiO_2 + \frac{x}{2}N_2$$
 (1)

When the temperature was above 650 °C, the silver powder in the silver paste dissolved into the molten glass frit in the form of  $Ag_2O$ . Then the dissolved  $Ag_2O$  diffused to the surface of Si and deposited metallic Ag on the Si emitter surface by the following reaction:

$$2Ag_2O + Si \rightarrow SiO_2 + 4Ag \tag{2}$$

The  $SiO_2$  produced in Equations (1) and (2) was incorporated into the molten glass frit. The Pb produced by Equation (1) would react with the dissolved  $Ag_2O$  or oxidize back to PbO by:

$$Ag_2O + Pb \rightarrow 2Ag + PbO \tag{3}$$

or:

$$2Pb + O_2 \rightarrow 2PbO \tag{4}$$

Simultaneously, the molten glass frit (glass layer) moved to the surface of Si with  $\mathrm{SiN}_{x}$  etched during the firing process, and Ag nanocrystals precipitated and distributed within the glass layer due to the lower solubility during the cooling process. The stagnant Ag powder aggregated to PADs on top of the glass layer during the firing and cooling processes in our work (Figure 1B).

Pt was subsequently electrodeposited on PADs (see Supporting Information) and the integrated Pt/PADs/Si component was ready to be used as a photocathode for water splitting (Figure 1C). The passivation and antireflection SiNx layer allows efficient light transmission and keeps the Si substrate away from the corrosive electrolyte (0.5 M H<sub>2</sub>SO<sub>4</sub>) (Figure 1D). Simultaneously, the glass layer under the PADs functions as the tunneling layer of photoexcited electrons, and offers corrosion resistance to the acidic electrolyte (Figure 1D). Moreover, the tunneling electrons further transfer from the conductive Ag dots to the catalytic Pt nanoparticles for hydrogen evolution reaction (HER) (Figure 1D). The PADs patterns were optimized and the photocathode showed a saturated photocurrent of 36.1 mA cm<sup>-2</sup> and a photovoltage of 0.61 V. The applied bias photo-tocurrent conversion efficiency (ABPE) reached 9.7%, and the photocurrent remained stable during the operation of 100 h at 0 V vs. reversible hydrogen electrode (RHE). The highperformance of the device is believed to result from the optimized light absorption and transfer of photoexcited electrons, and effective protection of the Si substrate. The photovoltaicelectrocatalytic (PV-EC) device is currently regarded as the

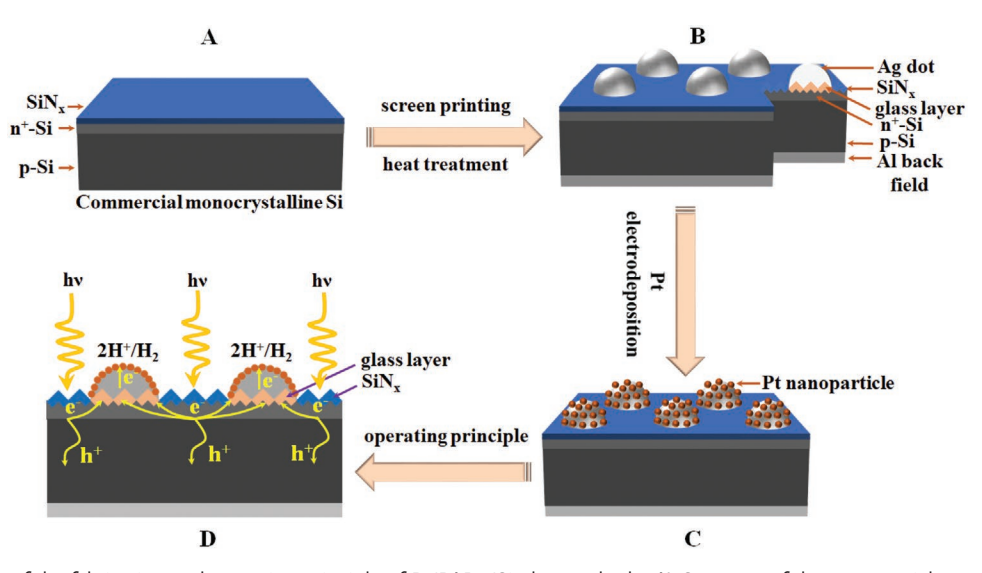


Figure 1. Schematic of the fabrication and operating principle of Pt/PADs/Si photocathode. A) Structure of the commercial monocrystalline  $p-n^+$  Si wafer with SiN<sub>x</sub> coating. B) Scaled-up manufacture of PADs/Si by screen printing and heat treatment on an Applied Baccini Soft Line. Ag dot: front electrode, Al: back field. C) Electrodeposition of Pt nanoparticles on PADs. D) The operating principle of Pt/PADs/Si photocathode for water splitting under light illumination.

www.afm-journal.de

16163028, 2022, 2, Downloaded from https://advanced.onlinelibrary.wiley.com/doi/10.1002/adfm.202107164 by University Town Of Shenzhen, Wiley Online Library on [23/1/2025]. See the Terms

on Wiley Online Library for rules of use; OA articles are governed by the applicable Creative Commons

most practical approach for solar-to-hydrogen conversion. For comparison, the PV-EC device, powered by one piece of Si solar cell and the identical Pt/AGLs configuration running HER, gave a saturation photocurrent of 36.9 mA cm $^{-2}$ , a photovoltage of 0.59 V, and an ABPE of 8.2%.

#### 2. Results and Discussion

#### 2.1. Material Characterizations

The photos of the PADs/Si, AGLs/Si, and typical connections to the PADs/Si photocathode and AGLs/Si solar cell are shown in Figure S1, Supporting Information. The schematic diagram of the Pt electrodeposition configuration on PADs and AGLs is exhibited in Figure S2, Supporting Information. The typical scanning electron microscopy (SEM) images of PADs/Si with different dot-spacings are shown in Figure S3, Supporting Information. Each Ag dot has a diameter of  $\approx \! 100~\mu m$  and they arrange in a hexagonal pattern (Figure S3, Supporting Information). Figure 2A shows the typical SEM morphology of the PADs/Si with a center-to-center dot-spacing of 0.75 mm (marked as d=0.75~mm) after Pt deposition. The PADs are completely covered by Pt nanoparticles and the diameter increases to about 126  $\mu m$  (Figures 2A and Figure S4, Supporting

Information). For the traditional AGLs, the line width is about 40  $\mu m$  and the spacing between two adjacent AGLs is about 1.5 mm (Figure S5, Supporting Information). The surface of AGLs is also rough like the PADs (Figures S3G and S5B, Supporting Information). The electrodeposited Pt nanoparticles cover the AGL completely, and spread out about 60  $\mu m$  from each side of the AGL (Figure S6, Supporting Information). The amorphous antireflection  $\mathrm{SiN}_x$  coating consists of micro domains as seen from the top view (Figure S7A,B, Supporting Information), and the surface structure of Si contains typical tetrahedron textures like pyramids for efficient light absorption (Figure S7C, Supporting Information). [38]

XRD on the PADs/Si wafer identifies the typical (111), (200), (220), (311), and (222) planes for Ag (PDF#04-0783) and Pt (PDF#04-0802) as shown in Figure S8, Supporting Information, respectively. The atomic interplanar distance of the nanoparticles as observed by transmission electron microscopy (TEM) and high-resolution TEM (HRTEM) is 2.27 Å which is consistent with that of (111) planes of cubic Pt (Figures 2B,C). The selected area electron diffraction (SAED) rings in the inset of Figure 2C corresponds to (111), (200), (220), and (222) crystal faces of cubic Pt. To further study the internal structure of PAD and AGL, an AGL sample was cut to ultrathin sheet by the focused ion beam (FIB) for HRTEM characterization (Figure S9A, Supporting Information). Fringes with a spacing of about 2.36 Å

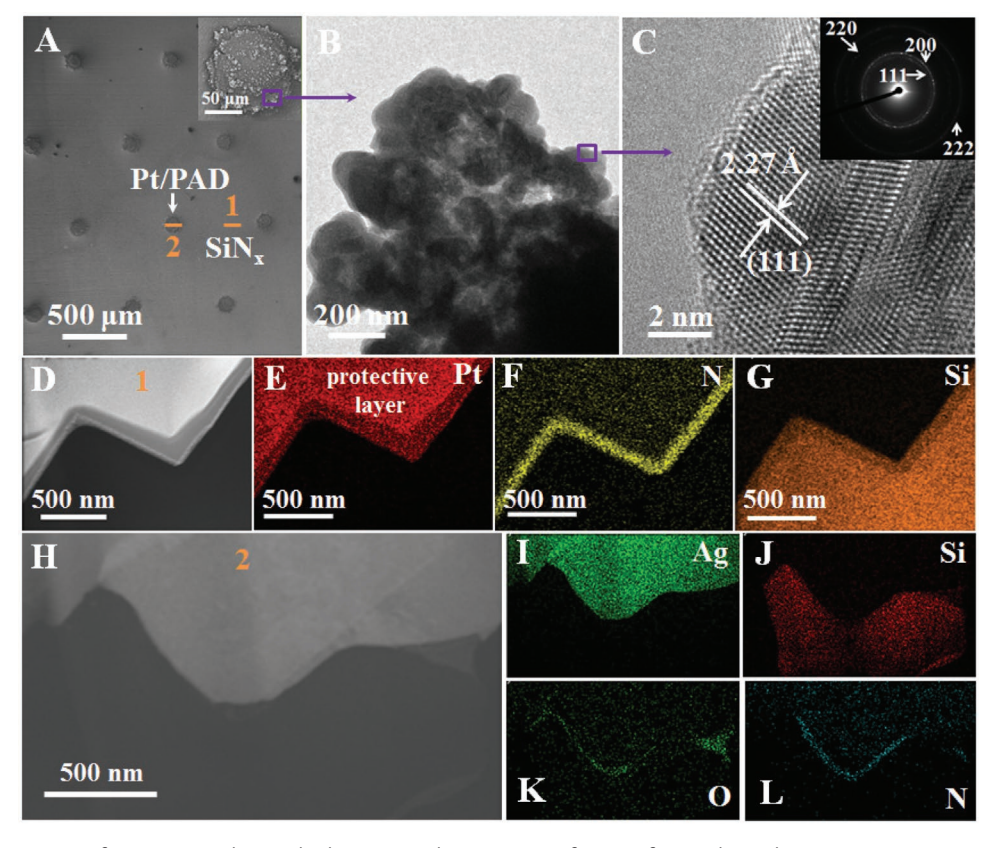


Figure 2. Characterizations of Pt/PADs/Si photocathode. A) Typical SEM image of PADs after Pt electrodeposition on monocrystalline p-n<sup>+</sup> Si wafer with  $SiN_x$  coating. Typical B) TEM and C) HRTEM images of the electrodeposited Pt nanoparticles (Inset in (C): SAED pattern). D) Scanning TEM (STEM) image of the cross-section of position 1 in (A). EDS element mapping of Pt (protective layer) (E), N (F), and Si (G) based on (D). H) STEM image of the cross-section of position 2 in (A). EDS element mapping of I) Ag, J) Si, K) O, and L) N based on (H).

www.afm-journal.de

1616298.2.222, 2, Downloaded from https://advanced.onlinelibrary.wiely.com/doi/10.102/affm.2021/0764 by University Town Of Shenzhen, Wiley Online Library on [2311/2025]. See the Terms and Conditions (https://onlinelibrary.wiely.com/terms-and-conditions) on Wiley Online Library for rules of use; OA articles are governed by the applicable Cerative Commons

identify that the (111) planes of Ag can be observed (Figure S9B, Supporting Information). The SAED pattern (the inset in Figure S9B, Supporting Information) further proves the cubic structure of Ag. The cross-section of  $SiN_x/Si$  (Figure 2D) was cut by FIB along the direction of Position 1 in Figure 2A. Pt was used to protect the material from FIB damages during the FIB cutting process (Figure 2E). The energy-dispersive X-ray spectroscopy (EDS) results indicate that the  $SiN_x$  layer is  $\approx 80$  nm in thickness and it homogenously covers the surface of the pyramid-like Si (Figures 2F,G).

The exposed glass-phase layer exhibits pothole morphology which results from the ablation of the Ag particles after stripping the AGL (Figure S10, Supporting Information).[39] The elements found in the region between the Pt layer (for protecting the material from FIB damages) and Si, including Ag, O, Pb, Bi, and Te, are within the glass layer of the AGL-stripped Si wafer (Figure S11, Supporting Information). The atomic ratio of O:Pb:Bi:Te is 46.35:1.98:1.57:1.22. There are still some Ag particles distribute along the surface of Si pyramid (Figure S11D, Supporting Information), and many other Ag particles are embedded inside the glass layer (Figure S12A, Supporting Information), as confirmed by the interplanar spacing of 2.04 Å from the (200) planes of cubic Ag (Figure S12B, Supporting Information). Actually, there are lots of Ag nanoparticles with different sizes in the glass layer observed from the enlarged image of Figure S12B, Supporting Information, which are marked in Figure S13, Supporting Information. The formation mechanism of Ag nanocrystals within the glass layer and on the surface of Si emitter has been discussed above.

In order to better understand the microstructure of the glass-phase layer, a cross-sectional sample (Figure 2H) for TEM characterization was cut by FIB through Pt/Ag/glass-layer/ Si along the direction of Position 2 in Figure 2A. During the firing process of Ag paste, the SiN<sub>x</sub> coating at the top of pyramid is nearly etched through by PbO to form the glass layer containing oxygen between PAD and Si (Figures 2I-K). However, the residual SiN<sub>x</sub> coating can still be observed, especially in the valley of the pyramid-shaped texture (Figure 2L).[40] Accordingly, the photoexcited electrons from Si are expected to migrate to AGLs and PADs by tunneling through Si contact/ thin-glass-layer/AGLs and PADs, or through multi-step tunneling through Si contact/thick-glass-layer/AGLs and PADs, in which the Si contact was constructed by Ag particles grown into the Si emitter.[39,40] Then the photoexcited electrons transfer from PADs to Pt catalyst for HER in Pt/PADs/Si photocathode (Figure 1D).

#### 2.2. PEC Performance

Typical PEC performance of the Pt-loaded PADs/Si photocathodes (**Figure 3**A) and the PV-EC device powered by one piece of AGLs/Si solar cell wafer was evaluated in 0.5 M  $\rm H_2SO_4$  with an exposed area of  $\approx 1~\rm cm^2$  under one sun illumination (AM 1.5G). In order to compare the performance under the identical condition for HER with PEC test, the electrodeposited Pt on AGLs (6  $\times$  1 cm) on the Si wafer with 1 cm² of exposed area was used as the working electrode for the performance test of PV-EC device (Figure 3B). Hereafter this device was marked as PV-EC

(Pt/AGLs). Note that the liquid level of electrolyte should be above the quartz window and the outside of the reactor should also be covered by rough black material to avoid any possible enhancement of incident light density by reflection during PEC performance tests. The electrocatalytic (EC) performance of the Pt/AGLs on the Si wafer with the same exposed area (1 cm²) was also measured under an external bias (Figure S14, Supporting Information). A commercial Pt mesh (1 cm²) was the counter electrode in above tests. Ar flow was applied to remove the oxygen in the electrolyte for one hour before performance test.

The photocurrent density-potential  $(J_{ph}-V)$  curves and dark current of the Pt/PADs/Si photocathode with different dot-spacings are shown in Figure 3C. The saturation photocurrent is 34.6 mA cm<sup>-2</sup> when the dot-spacing is 0.5 mm, and it increases to about 36.1 mA cm<sup>-2</sup> when the dot-spacings are 0.75 and 1.0 mm, then it further increases to 36.6 mA cm<sup>-2</sup> when the dot-spacing is 1.25 or 1.5 mm. Our reported saturation photocurrents are at the intermediate range compared with the previous results.[3,24,32-36,38,41-44] For further comparison. the saturation photocurrent is 35.8 mA cm<sup>-2</sup> based on the PEC performance of the Pt-loaded AGLs/Si (Pt/AGLs/Si) photocathode, which is close to the values of Pt/PADs/Si photocathodes (Figure S15A, Supporting Information and Figure 3C). It is worth noting that the saturation photocurrent of Pt/ AGLs/Si photocathode is lower than the short-circuit current (38.1 mA cm<sup>-2</sup>) when it was tested as an as-fabricated photovoltaic solar cell (Table S1, Supporting Information). The decreased photocurrent must result from the decreased incident light density due to electrolyte absorption, [45] H<sub>2</sub> bubble formation, and the defects formed during the laser cutting process compared with the as-fabricated Si solar cell in this work. [46] The calculated ABPE (Equation S1, Supporting Information) decreases from 9.7% to 6.7% for Pt/PADs/Si photocathodes with different dot-spacings (Figure 3D), and the ABPE is 6.9% for the Pt/AGLs/Si photocathode (Figure S15B, Supporting Information), which is close to that of Pt/PADs/Si (d = 1.5 mm) photocathode (Figure 3D). All the values are lower than the photovoltaic photon conversion efficiency (20.1%) as exhibited in Table S1, Supporting Information. For Si photocathodes, the lower efficiency results from the decreased incident light density caused by electrolyte absorption and/ or light-blocking catalysts, the recombination of photoexcited charges during the whole transport process through the device to the reduction catalysts, [45,47] and the mismatch between the slow surface HER reaction and the ultrafast light absorption through charge transfer.[48]

The PV-EC (Pt/AGLs) and Pt/AGLs/Si photocathode show a same onset potential (0.50 V) (Figures 3E and Figure S15A, Supporting Information), which was defined at the current density of 1 mA cm $^{-2}$ . [49] And both are lower than that (0.52 V) of Pt/PADs/Si ( $d=0.75\,$  mm) photocathode (Figure 3E). The onset potential is  $-0.09\,$  V vs. RHE for the EC water splitting of Pt/AGLs in 0.5 M  $\rm H_2SO_4$  (Figure 3E). Then the photovoltages are 0.59 and 0.61 V for PV-EC (Pt/AGLs) and Pt/AGLs/Si photocathode, and Pt/PADs/Si ( $d=0.75\,$  mm) photocathode, respectively. The saturation photocurrent is 36.9 mA cm $^{-2}$  for PV-EC (Pt/AGLs) (Figure 3E), which is higher than that (35.8 mA cm $^{-2}$ ) of Pt/AGLs/Si photocathode. The decreased photocurrent must be induced by the electrolyte

16163028, 2022, 2, Downloaded from https

hibrary.wiley.com/doi/10.1002/adfm.202107164 by University Town Of Shenzhen, Wiley Online Library on [23/11/2025]. See the Terms

and-conditions) on Wiley Online Library for rules of use; OA articles are governed by the applicable Creative Commons

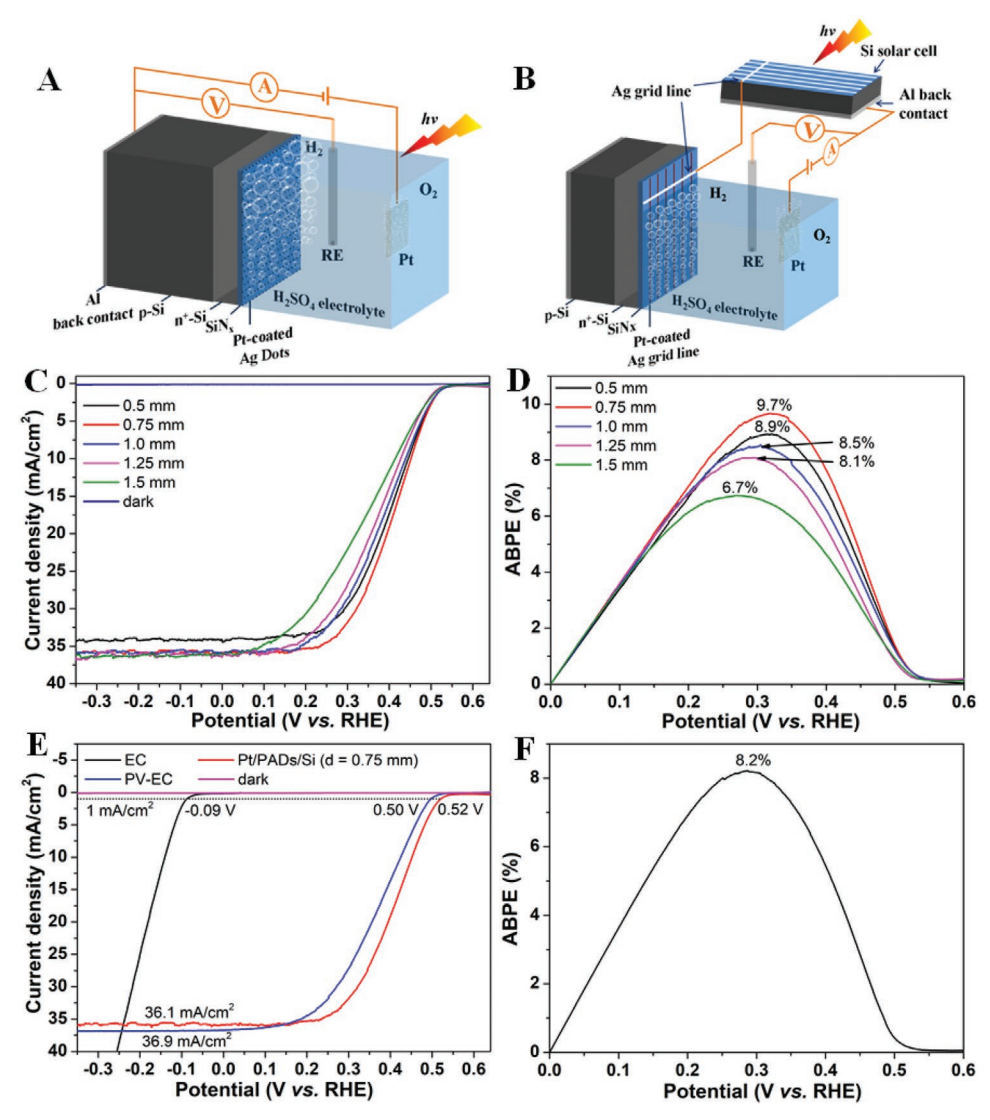


Figure 3. Performance of Pt/PADs/Si photocathodes with different dot-spacings and PV-EC (Pt/AGLs) for water splitting. Schematic pictures of A) Pt/PADs/Siphotocathodes and B) PV-EC (Pt/AGLs) (Working electrode: Pt-loaded AGLs (6×1cm)) for PEC water splitting. Counter electrode: Pt mesh (1 cm²); Electrolyte: 0.5 M H<sub>2</sub>SO<sub>4</sub> aqueous solution. C) Photocurrent density-potential ( $J_{ph}$ –V) curve under one sun illumination (AM 1.5G) and dark current of Pt/PADs/Si with different dot-spacings in 0.5 M H<sub>2</sub>SO<sub>4</sub> electrolyte. D) Variations of the applied-bias photon-to-current conversion efficiency (ABPE) for Pt/PADs/Si photocathodes. E) Photocurrent density-potential ( $J_{ph}$ –V) curve under one sun illumination (AM 1.5G) and dark current of the Pt/PADs/photocathode ( $J_{ph}$ –V) and PV-EC (Pt/AGLs), and the current density-potential ( $J_{ph}$ –V) of Pt-loaded AGLs (6×1 cm) for HER. Counter electrode: Pt mesh (1 cm²); Electrolyte: 0.5 M H<sub>2</sub>SO<sub>4</sub> aqueous solution. F) The applied-bias photon-to-current conversion efficiency (ABPE) for PV-EC (Pt/AGLs).

absorption and  $\rm H_2$  bubble formation as mentioned above. Additionally, the saturation photocurrent (36.9 mA cm<sup>-2</sup>) of PV-EC (Pt/AGLs) is lower than that ( $J_{\rm sc}=38.1$  mA cm<sup>-2</sup>) of the photovoltaic solar cell (Table S1, Supporting Information). This decreased photocurrent must be caused by the defects formed during the laser cutting process.<sup>[46]</sup> The calculated ABPE is 8.2% for PV-EC (Pt/AGLs) (Figure 3F), which is lower than that (9.7%) of the Pt/PADs/Si (d=0.75 mm) photocathode (Figure 3D).

Furthermore, the current and voltage at the maximum power point, and short-circuit current and open-circuit voltage for Pt/PADs/Si (d = 0.75 mm) photocathode and PV-EC (Pt/AGLs) are shown in Figure S16, Supporting Information. The calculated fill factors (ff) are 0.49 and 0.43 for the optimized PEC

and PV-EC (Pt/AGLs) water splitting (Equation S2, Supporting Information), respectively. In Figure 3E, it is obvious that Pt/PADs/Si (d=0.75 mm) photocathode and PV-EC (Pt/AGLs) system have reached their corresponding saturation photocurrents (36.1 and 36.9 mA cm<sup>-2</sup>) at the equilibrium water reduction potential ( $E^0$ ) in the acidic electrolyte (pH = 0), which is 0 V vs. RHE in this work. And the onset potentials ( $V_{\rm op}$ ) defined at current density of 1 mA cm<sup>-2</sup> are 0.52 and 0.50 V for Pt/PADs/Si (d=0.75 mm) photocathode and PV-EC (Pt/AGLs) system (Figure 3E), respectively. Based on the above data and Equation S3, Supporting Information, the calculated intrinsic solar-to-hydrogen conversion efficiency are 9.2% and 7.9% for Pt/PADs/Si (d=0.75 mm) photocathode and PV-EC

www.afm-journal.de

16163028, 2022. 2, Downloaded from https://advanced.onlinelibrary.wiley.com/doi/10.1002/adfm.202107164 by University Town Of Shenzhen, Wiley Online Library on [23/11/2025]. See the Terms and Conditions (https://onlinelibrary.wiley.com/doi/10.1002/adfm.202107164 by University Town Of Shenzhen, Wiley Online Library on [23/11/2025]. See the Terms and Conditions (https://onlinelibrary.wiley.com/doi/10.1002/adfm.202107164 by University Town Of Shenzhen, Wiley Online Library on [23/11/2025]. See the Terms and Conditions (https://onlinelibrary.wiley.com/doi/10.1002/adfm.202107164 by University Town Of Shenzhen, Wiley Online Library on [23/11/2025]. See the Terms and Conditions (https://onlinelibrary.wiley.com/doi/10.1002/adfm.202107164 by University Town Of Shenzhen, Wiley Online Library on [23/11/2025]. See the Terms and Conditions (https://onlinelibrary.wiley.com/doi/10.1002/adfm.202107164 by University Town Of Shenzhen, Wiley Online Library on [23/11/2025]. See the Terms and Conditions (https://onlinelibrary.wiley.com/doi/10.1002/adfm.202107164 by University Town Of Shenzhen, Wiley Online Library on [23/11/2025]. See the Terms and Conditions (https://onlinelibrary.wiley.com/doi/10.1002/adfm.202107164 by University Town Of Shenzhen, Wiley Online Library on [23/11/2025]. See the Terms and Conditions (https://onlinelibrary.wiley.com/doi/10.1002/adfm.202107164 by University Town Of Shenzhen, Wiley Online Library on [23/11/2025]. See the Terms and Conditions (https://onlinelibrary.wiley.com/doi/10.1002/adfm.202107164 by University Town Of Shenzhen, Wiley Online Library on [23/11/2025]. See the Terms and Conditions (https://onlinelibrary.wiley.com/doi/10.1002/adfm.202107164 by University Town Of Shenzhen, Wiley Online Library on [23/11/2025]. See the Terms and Conditions (https://onlinelibrary.wiley.com/doi/10.1002/adfm.202107164 by University Town Of Shenzhen, Wiley Online Library on [23/11/2025].

conditions) on Wiley Online Library for rules of use; OA articles are governed by the applicable Creative Commons

(Pt/AGLs) system, respectively. The Pt/PADs/Si (d=0.75 mm) photocathode obviously shows better performance than PV-EC (Pt/AGLs) and Pt/AGLs/Si photocathode for water splitting. Additionally, the PEC performance comparison of buried p-n junction silicon photocathodes is shown in Table S2, Supporting Information. Our optimized photocathode exhibits the highest photovoltage apart from intermediate performances in terms of photocurrent, ABPE, and stability.

Si solar cell-powered and commercial Pt-mesh catalyzed PV-EC device, marked as PV-EC (Pt meshes), can act as a reference for performance comparison (Figure S17, Supporting Information). Its saturation photocurrent (36.9 mA cm $^{-2}$ ) is same as that of PV-EC (Pt/AGLs) (Figures 3E and Figure S18A, Supporting Information). However, its onset potential (0.53 V) is higher than those of Pt/PADs/Si ( $d=0.75\,\mathrm{mm}$ ) photocathode and PV-EC (Pt/AGLs). And it shows an ABPE of 9.5% (Figure S18B, Supporting Information), a little lower than that (9.7%) of Pt/PADs/Si ( $d=0.75\,\mathrm{mm}$ ) photocathode.

# 2.3. Mechanism of Enhanced Performance for Optimal Photocathode

Based on the SEM results (Figures S1D and S5A, Supporting Information), the width of each AGL is about 40  $\mu m$ , and there are six AGLs on the  $1\times1~cm^2$  Si solar cell wafer. Thus the calculated fraction of the surface covered by AGLs is about 2.4% on AGLs/Si solar cell wafer (Table S3, Supporting Information). For PADs/Si photocathode, there are different number of line and number of dot per line for different PAD dot-spacings on  $3\times3~cm^2$  Si wafer (Table S4, Supporting Information), and the

single dot area is about  $7.85 \times 10^{-3}$  mm<sup>2</sup>. Then the surface covered ratio can be calculated according to above data. For PADs/ Si (d = 0.5 mm) photocathode, the fraction of covered surface is 3.7% (Table S4, Supporting Information). Apparently, the PADs/ Si (d = 0.5 mm) photocathode blocks a larger surface area of the Si wafer than AGLs/Si solar cell wafer. Accordingly, the saturation photocurrent (34.6 mA cm<sup>-2</sup>) of Pt/PADs/Si (d = 0.5 mm) photocathode is lower than that (35.8 mA cm<sup>-2</sup>) of Pt/AGLs/Si photocathode (Figures 3C and Figure S15A, Supporting Information) due to the less efficient light absorption. Furthermore, the fraction of covered surface decreases from 1.7% to 0.4% when the dot-spacing increases from 0.75 to 1.5 mm (Table S4, Supporting Information). The saturation photocurrent for Pt/PADs/ Si increases to about 36.1 mA cm<sup>-2</sup> as d = 0.75 or 1.0 mm, and it further increases to around 36.6 mA cm<sup>-2</sup> as d = 1.25 or 1.5 mm (Figure 3C). These results demonstrate that a smaller blocked surface area is beneficial to increase the saturated photocurrent. Additionally, Pt/PADs/Si (d = 0.75 mm) photocathode shows the highest photocurrent at the low external bias range (Figure 3C), which must be caused by the more efficient collection of photo excited electrons. It can be concluded that d = 0.75 mm is the optimal dot-spacing owing to the balance between surface coverage (covered ratio: 1.7%) and collection of photoexcited electrons, leading to the best PEC performance in terms of ABPE for Pt/PADs/Si photocathode in this work.

The schematic band diagram and Nyquist impedance tests in **Figure 4** explain the reasons resulting in different performances between Pt/PADs/Si (d = 0.75 mm) photocathode and PV-EC (Pt/AGLs) system for water splitting. They show the same band diagram except additional external wire for PV-EC (Pt/AGLs), which may cause voltage loss (Figures 4A,B). According to the

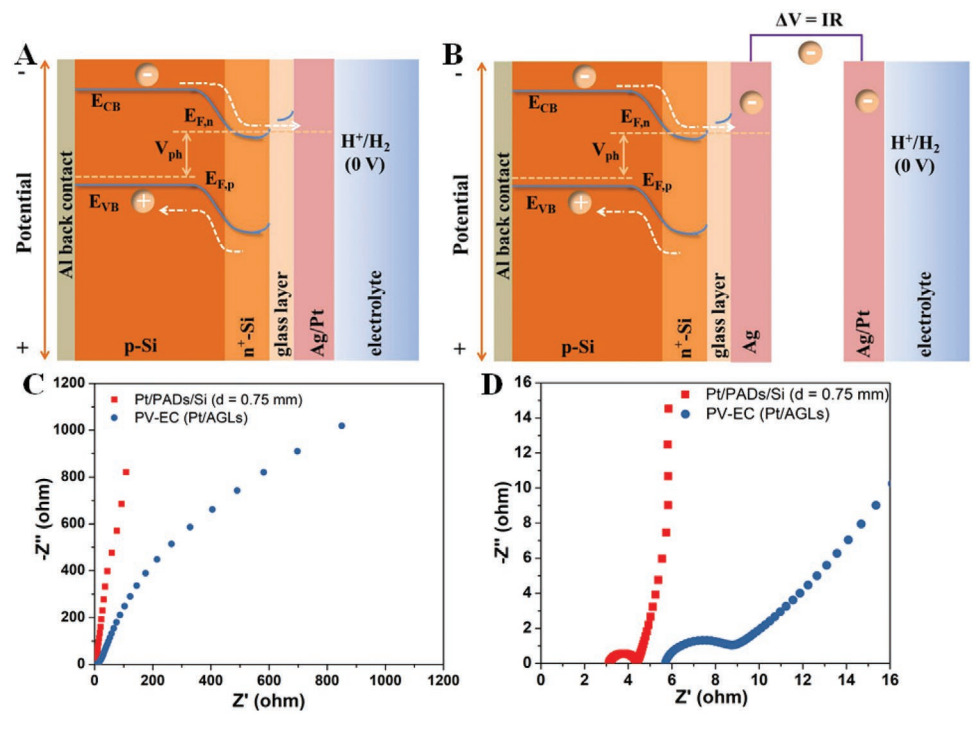


Figure 4. Schematic band diagram of A) Pt/PADs/Si photocathodes and B) PV-EC (Pt/AGLs) for water splitting. C) Nyquist impedance plots of Pt/PADs/Si (d = 0.75 mm) photocathode and PV-EC (Pt/AGLs) measured under illumination and D) the magnified picture in the high-frequency range.

16163028, 2022, 2, Downloaded from https

elibrary.wiley.com/doi/10.1002/adfm.202107164 by University Town Of Sherzhen, Wiley Online Library on [23/11/2025]. See the Terms and Conditions (https://onlinelibrary.wiley

and-conditions) on Wiley Online Library for rules of use; OA articles are governed by the applicable Creative Commons

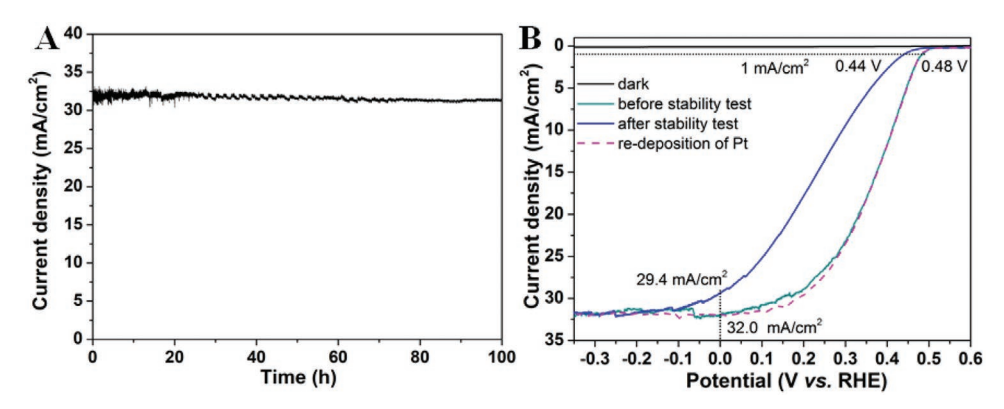


Figure 5. Stability test of Pt/PADs/Si (d = 0.75 mm) photocathode for water splitting. A) Stability measurement of the Pt/PADs/Si (d = 0.75 mm) photocathode by the steady-state photocurrent at 0 V vs. RHE under 100 mW cm<sup>-2</sup> illumination in 0.5 M H<sub>2</sub>SO<sub>4</sub> at 25 °C. B) Photocurrent density-potential ( $J_{ph}$ –V) curve and dark current of Pt/PADs/Si (d = 0.75 mm) photocathode (before stability test, after stability test for 100 h, and re-deposition of Pt catalyst) measured in 0.5 M H<sub>2</sub>SO<sub>4</sub> electrolyte under one sun illumination (AM 1.5G).

magnified picture (Figure 4D) in the high-frequency range based on the whole Nyquist impedance plots under illumination (Figure 4C), Pt/PADs/Si (d = 0.75 mm) photocathode exhibits about 3  $\Omega$  of series resistance, which is smaller than that (about 5.7  $\Omega$ ) for PV-EC (Pt/AGLs). This result is consistent with the fact that PV-EC (Pt/AGLs) has external wire with additional resistance. Simultaneously, they all show well-defined semicircle in the highfrequency range, the diameter of which corresponds to the charge transfer resistance and a lower resistance means a faster reaction rate. Apparently, the Pt/PADs/Si (d = 0.75 mm) photocathode leads to a lower charge transfer resistance, implying faster electrode kinetics for HER than PV-EC (Pt/AGLs). In the middle and low-frequency range as shown in Figure 4C, the angles between the Nyquist impedance plot of Pt/PADs/Si (d = 0.75 mm) photocathode and Z' axis are larger than those for PV-EC (Pt/AGLs). It means that the protons are easier to diffuse to the reaction surface of Pt/PADs/Si (d = 0.75 mm) photocathode for HER. It can be concluded that the absence of external resistance, faster electrode kinetics, and easier diffusion of protons to reaction surface for HER make Pt/PADs/Si (d = 0.75 mm) photocathode exhibit better performance than PV-EC (Pt/AGLs).

In Figure S19, Supporting Information, the commercial Pt mesh (1 cm²) for HER exhibits a lower overpotential (–0.096 V) than that (–0.141 V) of Pt/AGLs at the current density of 10 mA cm² besides the higher current density during the test. Nyquist impedance plots for the two catalysts (Figure S20, Supporting Information) also show well-defined semicircles, and the Pt mesh (1 cm²) leads to faster electrode kinetics for HER. This result can explain why Pt/AGLs need a higher overpotential to achieve the same current density compared with Pt mesh, and thus explain the reason for that PV-EC (Pt meshes) shows better performance than PV-EC (Pt/AGLs).

### 2.4. PEC Stability of Pt/PADs/Si (d = 0.75 mm) Photocathode

The stability of the photocathode was measured in a glass reactor with a quartz side-window, and this reactor was connected to a circulating cooling system. The photocurrent of Pt/PADs/Si (d = 0.75 mm) does not degrade noticeably after 100 h of operation with a photocurrent around (31.0 ± 1.0) mA cm<sup>-2</sup>

at 0 V vs. RHE and 25 °C (Figure 5A). The decreased onset potential (0.48 V) and saturation photocurrent (32.0 mA cm $^{-2}$ ) during the stability test are lower than those (0.52 V and 36.1 mA cm $^{-2}$ ) during the PEC evaluation in Figure 3E. It must be caused by the stronger absorption of the incident light by electrolyte in the stability measurement reactor. After the stability test, the PEC performance becomes poorer than the as-prepared photocathode (Figure 5B). The onset potential at 1 mA cm $^{-2}$  is negatively shifted from 0.48 to 0.44 V vs. RHE, and the photocurrent decreases from  $\approx$ 32.0 to 29.4 mA cm $^{-2}$  at 0 V vs. RHE (Figure 5B). However, the PEC performance completely recovers when the Pt was re-electrodeposited using the same method (Figure 5B).

Further characterizations of the Pt/PADs/Si (d = 0.75 mm) photocathode after the stability test were carried out. SEM of the surface morphology suggests that the SiN<sub>r</sub> coating still covers the Si wafer densely (Figure S21, Supporting Information). The SEM morphology of the AGL-stripped glass layer immersed in 0.5 M H<sub>2</sub>SO<sub>4</sub> for 100 h shows no obvious changes in comparison with the original one (Figures S10 and S22, Supporting Information). The EDS mapping indicates the Ag, O, Pb, Bi, and Te can be obviously detected in the glass layer treated in 0.5 M H<sub>2</sub>SO<sub>4</sub> for 100 h (Figure S23, Supporting Information). The molar ratio of O:Pb:Bi:Te was 46.05:1.79:1.31:1.23, and it was similar to that before the aqueous H<sub>2</sub>SO<sub>4</sub> treatment. The stable morphology and composition demonstrate that the glass layer was resistant to the corrosion by H2SO4. Though the morphology of the Pt catalyst did not exhibit obvious change after the stability measurement when compared with the as-prepared sample (Figures 2A and Figures S4 and S24, Supporting Information), it has been observed that Pt easily leaves the photocathode during HER process.<sup>[50]</sup> Based on the above analysis and experimental results, it can be concluded that the left-shift of the  $I_{ph}$ -V curve after the stability test resulted from the loss of Pt catalyst from the PADs.

#### 3. Conclusion

This work presents a scalable manufacture strategy for the fabrication of photocathode with PADs on the commercial

www.afm-journal.de

1616280.2.022, 2, Downloaded from https://da/accedonlinelibrary.wiely.com/oi/10.102/adfrm.20210110.64 by University Town Of Shenzhen, Wiley Online Library on [23/11/2025]. See the Terms and Conditions (https://onlinelibrary.viely.com/terms-and-conditions) on Wiley Online Library for rules of use; OA articles are governed by the applicable Centarie Commons and Conditions (https://onlinelibrary.viely.com/terms-and-conditions) on Wiley Online Library for rules of use; OA articles are governed by the applicable Centarie Commons and Conditions (https://onlinelibrary.viely.com/terms-and-conditions) on Wiley Online Library for rules of use; OA articles are governed by the applicable Centarie Commons and Conditions (https://onlinelibrary.viely.com/terms-and-conditions) on Wiley Online Library for rules of use; OA articles are governed by the applicable Centarie Commons and Conditions (https://onlinelibrary.viely.com/terms-and-conditions) on Wiley Online Library for rules of use; OA articles are governed by the applicable Centarie Commons and Conditions (https://onlinelibrary.viely.com/terms-and-conditions) on Wiley Online Library for rules of use; OA articles are governed by the applicable Centarie Commons and Conditions (https://onlinelibrary.viely.com/terms-and-conditions) on Wiley Online Library for rules of use; OA articles are governed by the applicable Centaries (https://onlinelibrary.viely.com/terms-and-conditions) on the applicable Centaries

www.advancedsciencenews.com

crystalline p-n+ Si with a SiNx coating, which is totally compatible with the Si solar cell fabrication industry. We found a new combination of multifunctional spatial-decoupling light absorption layer (SiN<sub>x</sub>) and catalytic reaction (glass layer/Ag/Pt) sites for Si photocathode to achieve high efficiency in an acidic electrolyte. Though the stability of the integrated Pt/PADs/Si photocathode was jeopardized by the leaving of electrodeposited Pt from PADs, the protection and electron tunneling layers (SiN<sub>x</sub> and glass layers) are very stable in the H<sub>2</sub>SO<sub>4</sub> electrolyte. The PEC performance was controlled by the balance between the light absorption and the collection of photoexcited electrons. Our results for the first time discover that the optimized Pt/PADs/Si (d = 0.75 mm) photocathode is more efficient than PV-EC device for water splitting. The performance of the integrated photocathode could be further improved by optimizing the diameter of Ag dot and dot-spacing of PADs, and adopting better Pt deposition routes to improve its contact on PADs for improved stability, such as electron beam evaporation or magnetron sputtering approach with appropriate mask. This work provides a promising route to make Si photocathode commercially viable.

# **Supporting Information**

Supporting Information is available from the Wiley Online Library or from the author.

## Acknowledgements

The research was financially supported by National Key R&D Program of China (2016YFB0700600), the Guangdong Innovation Team Project (No. 2013N080), Soft Science Research Project of Guangdong Province (No. 2017B030301013), Shenzhen Science and Technology Research Grant (ZDSYS201707281026184), Chemistry and Chemical Engineering Guangdong Laboratory (Grant No.1922018).

#### **Conflict of Interest**

The authors declare no conflict of interest.

#### **Data Availability Statement**

Research data are not shared.

#### Keywords

industrial strategies, multifunctional layers, Si photocathodes, spatial decoupling layers

Received: July 23, 2021 Revised: September 18, 2021 Published online: October 7, 2021

- [1] M. J. Kenney, M. Gong, Y. Li, J. Z. Wu, J. Feng, M. Lanza, H. Dai, Science 2013, 342, 836.
- [2] Y. Yu, Z. Zhang, X. Yin, A. Kvit, Q. Liao, Z. Kang, X. Yan, Y. Zhang, X. Wang, Nat. Energy 2017, 2, 17045.

- [3] L. Ji, M. D. Mcdaniel, S. Wang, A. B. Posadas, X. Li, H. Huang, J. C. Lee, A. A. Demkov, A. J. Bard, J. G. Ekerdt, E. T. Yu, Nat. Nanotechnol. 2015, 10, 84.
- [4] Y. Wang, W. Tian, C. Chen, W. Xu, L. Li, Adv. Funct. Mater. 2019, 29, 1809036.
- [5] P. Sharma, J. W. Jang, J. S. Lee, ChemCatChem 2019, 11, 157.
- [6] J. H. Kim, J. S. Lee, Adv. Mater. 2019, 31, 1806938.
- [7] J. Seo, H. Nishiyama, T. Yamada, K. Domen, Angew. Chem., Int. Ed. 2018, 57, 8396.
- [8] S. Chandrasekaran, L. Yao, L. Deng, C. Bowen, Y. Zhang, S. Chen, Z. Lin, F. Peng, P. Zhang, Chem. Soc. Rev. 2019, 48, 4178.
- [9] D. K. Lee, D. Lee, M. A. Lumley, K. S. Choi, Chem. Soc. Rev. 2019, 48, 2126.
- [10] W. Yang, J. Moon, ChemSusChem 2019, 12, 1889.
- [11] S. Otep, T. Michinobu, Q. Zhang, Sol. RRL 2020, 4, 1900395.
- [12] S. Bellani, M. R. Antognazza, F. Bonaccorso, Adv. Mater. 2019, 31, 1801446.
- [13] H. Zhang, Z. Yang, W. Yu, H. Wang, W. Ma, X. Zong, C. Li, Adv. Energy Mater. 2018, 8, 1800795.
- [14] A. Mezzetti, F. Fumagalli, A. Alfano, D. Iadicicco, M. R. Antognazza, F. Di Fonzo, Faraday Discuss. 2017, 198, 433.
- [15] Q. Ding, L. Gou, D. Wei, D. Xu, W. Fan, W. Shi, Int. J. Hydrogen Energy 2021, 46, 24965.
- [16] J. Seo, H. J. Kim, R. T. Pekarek, M. J. Rose, J. Am. Chem. Soc. 2015, 137, 3173.
- [17] Y. J. Dong, J. F. Liao, Z. C. Kong, Y. F. Xu, Z. J. Chen, H. Y. Chen, D. Bin Kuang, D. Fenske, C. Y. Su, Appl. Catal., B 2018, 237, 9.
- [18] W. Shi, W. Yu, D. Li, D. Zhang, W. Fan, J. Shi, C. Li, Chem. Mater. 2019, 31, 1928.
- [19] W. Shi, D. Li, W. Fan, J. Ma, C. Li, W. Yu, J. Shi, C. Li, Adv. Funct. Mater. 2020, 30, 2003399.
- [20] C. Dai, T. He, L. Zhong, X. Liu, W. Zhen, C. Xue, S. Li, D. Jiang, B. Liu, Adv. Mater. Interfaces 2021, 8, 2002191.
- [21] X. L. Zheng, J. P. Song, T. Ling, Z. P. Hu, P. F. Yin, K. Davey, X. W. Du, S. Z. Qiao, Adv. Mater. 2016, 28, 4935.
- [22] K. Yoshikawa, H. Kawasaki, W. Yoshida, T. Irie, K. Konishi, K. Nakano, T. Uto, D. Adachi, M. Kanematsu, H. Uzu, K. Yamamoto, Nat. Energy 2017, 2, 17032.
- [23] J. Yang, J. K. Cooper, F. M. Toma, K. A. Walczak, M. Favaro, J. W. Beeman, L. H. Hess, C. Wang, C. Zhu, S. Gul, J. Yano, C. Kisielowski, A. Schwartzberg, I. D. Sharp, *Nat. Mater.* 2017, 16, 335.
- [24] M. Cabán-Acevedo, M. L. Stone, J. R. Schmidt, J. G. Thomas, Q. Ding, H. C. Chang, M. L. Tsai, H. He, S. Jin, *Nat. Mater.* 2015, 14, 1245.
- [25] J. C. Hill, A. T. Landers, J. A. Switzer, Nat. Mater. 2015, 14, 1150.
- [26] D. V. Esposito, I. Levin, T. P. Moffat, A. A. Talin, *Nat. Mater.* 2013, 12, 562.
- [27] A. G. Scheuermann, J. P. Lawrence, K. W. Kemp, T. Ito, A. Walsh, C. E. D. Chidsey, P. K. Hurley, P. C. McIntyre, Nat. Mater. 2016, 15, 99.
- [28] Y. W. Chen, J. D. Prange, S. Dühnen, Y. Park, M. Gunji, C. E. D. Chidsey, P. C. McIntyre, Nat. Mater. 2011, 10, 539.
- [29] S. Hu, M. R. Shaner, J. A. Beardslee, M. Lichterman, B. S. Brunschwig, N. S. Lewis, Science 2014, 344, 1005.
- [30] C. U. Maier, M. Specht, G. Bilger, Int. J. Hydrogen Energy 1996, 21, 859.
- [31] K. Sun, N. Park, Z. Sun, J. Zhou, J. Wang, X. Pang, S. Shen, S. Y. Noh, Y. Jing, S. Jin, P. K. L. Yu, D. Wang, Energy Environ. Sci. 2012, 5, 7872.
- [32] B. Liu, S. Feng, L. Yang, C. Li, Z. Luo, T. Wang, J. Gong, Energy Environ. Sci. 2020, 13, 221.
- [33] W. Vijselaar, P. Westerik, J. Veerbeek, R. M. Tiggelaar, E. Berenschot, N. R. Tas, H. Gardeniers, J. Huskens, Nat. Energy 2018, 3, 185.
- [34] H. C. Fu, P. Varadhan, C. H. Lin, J. H. He, Nat. Commun. 2020, 11, 3930.
- [35] S. K. Karuturi, H. Shen, A. Sharma, F. J. Beck, P. Varadhan, T. Duong, P. R. Narangari, D. Zhang, Y. Wan, J. H. He,





www.afm-journal.de

16163028, 2022, 2, Downloaded

onlinelibrary.wiley.com/doi/10.1002/adfm.202107164 by University Town Of Shenzhen, Wiley Online Library on [23/11/2025]

l. See

governed by the applicable Creative Commons

- H. H. Tan, C. Jagadish, K. Catchpole, Adv. Energy Mater. 2020, 10, 2000772.
- [36] H. C. Fu, P. Varadhan, M. L. Tsai, W. Li, Q. Ding, C. H. Lin, M. Bonifazi, A. Fratalocchi, S. Jin, J. H. He, Nano Energy 2020, 70, 104478.
- [37] J. D. Fields, I. Ahmad, V. L. Pool, J. Yu, D. G. Van Campen, P. A. Parilla, M. F. Toney, M. F. A. M. Van Hest, *Nat. Commun.* 2016, 7, 11143.
- [38] C. K. Ku, P. H. Wu, C. C. Chung, C. C. Chen, K. J. Tsai, H. M. Chen, Y. C. Chang, C. H. Chuang, C. Y. Wei, C. Y. Wen, T. Y. Lin, H. L. Chen, Y. S. Wang, Z. Y. Lee, J. R. Chang, C. W. Luo, D. Y. Wang, B. J. Hwang, C. W. Chen, Adv. Energy Mater. 2019, 9, 1901022.
- [39] E. Cabrera, S. Olibet, J. Glatz-Reichenbach, R. Kopecek, D. Reinke, G. Schubert, *Energy Procedia* 2011, 8, 540.
- [40] C. H. Lin, S. Y. Tsai, S. P. Hsu, M. H. Hsieh, Sol. Energy Mater. Sol. Cells 2008, 92, 1011.
- [41] H. Li, B. Liu, S. Feng, H. Li, T. Wang, J. Gong, J. Mater. Chem. A 2020, 8, 224.

- [42] Z. Yin, R. Fan, G. Huang, M. Shen, Chem. Commun. 2018, 54, 543.
- [43] R. Fan, J. Zhou, W. Xun, S. Cheng, S. Vanka, T. Cai, S. Ju, Z. Mi, M. Shen, *Nano Energy* 2020, 71, 104631.
- [44] B. Liu, S. Wang, S. Feng, H. Li, L. Yang, T. Wang, J. Gong, Adv. Funct. Mater. 2020, 31, 2007222.
- [45] H. Döscher, J. F. Geisz, T. G. Deutsch, J. A. Turner, Energy Environ. Sci. 2014, 7, 2951.
- [46] M. D. Abbott, J. E. Cotter, F. W. Chen, T. Trupke, R. A. Bardos, K. C. Fisher, J. Appl. Phys. 2006, 100, 114514.
- [47] H. P. Wang, K. Sun, S. Y. Noh, A. Kargar, M. L. Tsai, M. Y. Huang, D. Wang, J. H. He, *Nano Lett.* **2015**, *15*, 2817.
- [48] Z. Wang, L. Wang, Chin. J. Catal. 2018, 39, 369.
- [49] R. Fan, W. Dong, L. Fang, F. Zheng, M. Shen, J. Mater. Chem. A 2017, 5, 18744.
- [50] R. Fan, C. Tang, Y. Xin, X. Su, X. Wang, M. Shen, Appl. Phys. Lett. 2016, 109, 233901.